Article

Use of Hydrothermal Carbonization and Cold Atmospheric Plasma for Surface Modification of Brewer's Spent Grain and Activated Carbon

Krystian Krochmalny [1,*], Halina Pawlak-Kruczek [1], Norbert Skoczylas [2], Mateusz Kudasik [2], Aleksandra Gajda [2], Renata Gnatowska [3], Monika Serafin-Tkaczuk [1], Tomasz Czapka [1], Amit K. Jaiswal [4], Vishwajeet [1], Amit Arora [5], Tomasz Hardy [1], Mateusz Jackowski [1], Michał Ostrycharczyk [1] and Łukasz Niedźwiecki [1]

1 Faculty of Mechanical and Power Engineering, Department of Energy Conversion Engineering, Wroclaw University of Science and Technology, 50-370 Wroclaw, Poland; halina.pawlak@pwr.edu.pl (H.P.-K.); monika.tkaczuk@pwr.edu.pl (M.S.-T.); tomasz.czapka@pwr.edu.pl (T.C.); vishwajeet.na@pwr.edu.pl (V.); tomasz.hardy@pwr.edu.pl (T.H.); mateusz.jackowski@pwr.edu.pl (M.J.); michal.ostrycharczyk@pwr.edu.pl (M.O.); lukasz.niedzwiecki@pwr.edu.pl (Ł.N.)
2 The Strata Mechanics Research Institute of the Polish Academy of Sciences, 30-059 Kraków, Poland; skoczylas@imgpan.pl (N.S.); kudasik@imgpan.pl (M.K.); aleksandra.gajda@imgpan.pl (A.G.)
3 Faculty of Mechanical Engineering and Computer Science, Institute of Thermal Machinery, Częstochowa University of Technology, Armii Krajowej 21, 42-200 Częstochowa, Poland; renata.gnatowska@pcz.pl
4 School of Food Science and Environmental Health, Faculty of Science, Technological University Dublin-City Campus, Central Quad, Grangegorman, D07 ADY7 Dublin, Ireland; amit.jaiswal@TUDublin.ie
5 Department of Chemical Engineering, Shaheed Bhagat Singh State University, Ferozepur 152004, Punjab, India; amitarora@sbsstc.ac.in or aroraamitlse@yahoo.com
* Correspondence: krystian.krochmalny@pwr.edu.pl

Abstract: This paper presents results that show the effect of hydrothermal carbonization and subsequent cold plasma jet treatment with helium and argon on the structure and sorption properties of a material—spent brewery grain. Treatment of activated carbon, with a cold atmospheric plasma jet, was used comparatively. The effect of activation on the pore structure of the materials was carried out by the volumetric method at low pressure (N_2, 77 K). The specific surface area as well as the total pore volume, average pore size, and pore size distribution were determined using different theoretical models. A high improvement in the sorption capacity parameter was obtained for hydrochars after cold atmospheric plasma jet treatment with an increase of 7.5 times (using He) and 11.6 times (using Ar) compared with hydrochars before cold atmospheric plasma jet treatment. The increase in specific surface area was five-fold (He) and fifteen-fold (Ar). For activated carbon, such a large change was not obtained after plasma activation. Regardless of the gas used, the increase in structural parameter values was 1.1–1.3.

Keywords: plasma; biomass; brewer's spent grain; activation; HTC; structure; pore size distribution

1. Introduction

Beer is brewed all around the world and has been throughout the years. World beer production in 2020 amounted to 1.82 billion hectoliters [1]. Because the shares of beer, wine, and spirits consumption in OECD (Organization for Economic Co-operation and Development) countries appear to be leveling off, it is plausible to expect that the aforementioned consumption will not decline in the following decades [2]. Brewer's Spent Grain (BSG) is the main residue from beer brewing [3]. BSG is an organic residue, with relatively low ash content [3]. This could make it a suitable feedstock for the production of activated carbons [3]. However, its relatively high moisture content, reaching 70–75% [3,4], is a serious obstacle in its use as a feedstock for the production of activated carbon due to drying being an energy-intensive process.

Hydrothermal carbonization (HTC) seems a promising technique for the valorization of BSG [5,6]. It is a thermal valorization process carried out in subcritical water at enhanced pressure and at elevated temperatures (usually 200 to 260 °C) [7–11]. The ionic constant of water increases dramatically at temperatures between 200 and 280 °C, and water begins to behave as a non-polar solvent [12]. The process involves multiple reactions that generate multiple different products using complex raw materials, i.e., various kinds of biomass [13,14]. The HTC process begins with hydrolysis, which decomposes biomass into different amounts of monomers and oligomers [14], along with a few intermediates, such as 2-furfural, and 5-hydroxymethyl furfural (5-HMF) [14,15]. The rate of hydrolysis is diffusion-controlled, according to the literature, and is thus limited by transport phenomena inside the fibrous structure of biomass [16]. Therefore, an increase in the temperature increases the hydrolysis rate [17–19]. Dehydration and decarboxylation occur after hydrolysis [14,15,20]. The number of hydroxyl groups (OH) decrease during dehydration [14]. Colloidal structures are degraded, resulting in a reduction in the number of hydrophilic groups, which promotes the generation of gases (mainly CO_2) [13]. A few more gases are produced, such as CO, CH_4, and H_2 (in the case of a catalytic process) [17,18]. A lower O/C ratio is reported because of the decrease in the amount of OH groups. Decarboxylation results in a decrease in the amount of carboxyl (COOH) and carbonyl (C=O) groups, also slightly decreasing the O/C ratio of the solid product [14]. This is then followed by polymerization as well as aromatization [14,15].

The decrease in the amount of hydroxyl groups causes hydro-thermally carbonized biomass to become more hydrophobic, resulting in a significant reduction in the equilibrium moisture content [21] hence making physical dewatering easier [14]. This is reported for various types of biomass [22,23]. The liquid fraction can be purified [24,25] and used for the production of biogas [26,27]. Moreover, the process of hydrothermal carbonization results in improvements in combustion [28], increasing the grindability of the processed biomass as well as enhancing the biomass regarding composition of an inorganic fraction [13,29]. Some studies have revealed the easier pelletizing of hydrochars compared with raw biomass [30–32].

The applicability of a material as a sorbent is mainly determined by its structural properties. The development of effective sorbents of natural and anthropogenic origin, which are characterized by a high specific surface area and an optimum pore distribution, has been extensively studied. Sorbents based on biomass and biochar are the subject of numerous studies. They are used to monitor mercury emissions from gases [33] and greenhouse gases (GHG) [34]. To obtain an effective raw material for GHG capture, calcination of the mineral halloysite was carried out in the work [35]. Some GHG removal studies were carried out using modified calcium-based and soda-based sorbents [36,37]. In works [38–40] carbon materials were compared with other natural and synthetic materials in terms of hydrogen and GHG sorption efficiency.

Activated carbons belong to one of the most widely used groups of carbon sorbents. The multitude of origins of activated carbons and their high efficiency make them used in almost all fields of gas and liquid purification. Intensive investigations on novel feedstocks and methods of production of activated carbon (AC) are very useful from the perspective of the cost of state-of-the-art technology [41]. A plant, using the steam activation process, producing activated carbon from pecan nutshells, requires more than 2.1 million USD of total investment cost for a plant with an approximate annual output of 450 tons [41]. On the other hand, a plant using a similar amount of feedstock and phosphoric acid activation, with an annual output of approximately 960 tons, could cost as much as USD 6.3 million [41], owing it to a higher amount of unit operations, thus adding to the cost of additional devices (rotary driers and H_3PO_4 washing stages [41]). Such high investment cost can be attributed to the number of unit operations as well as to the size of the processing units, determined by the required residence time, which is in the order of 1 h in the case of both carbonization and activation [41]. The annual operating cost can be as high as USD 1.2 and 2.8 million for steam and phosphoric acid activation, respectively [41], whereas labor

cost is approximately 30% of the annual operating cost for steam activation and 20% for the plants, where phosphoric acid is used [41].

The use of plasma for activation gives the benefit of high energy density, which results in much shorter residence times needed for activation, in comparison to traditional activation techniques [42]. This could result in CAPEX reduction, due to decreased bulk size of the activation installation, and a simplified and modular design. The latter could also bring benefits in terms of logistics, as a modular character makes such installation feasible on a smaller scale, closer to the source of residues, thus decreasing the cost involved with transportation. By far the biggest advantage of using plasma for activation purposes is its potential regarding functionalization of the surface. Che, Zhou and Wang [27] successfully modified the surface of viscose-based activated carbon fibers to improve the adsorption of SO_2, using dielectric barrier discharge plasma (DBD), with N_2 [27]. Treatment resulted in better adsorption capacity, due to forming of nitrogen groups on the surface [27]. Wu et al. [28] modified activated carbon using DBD plasma and the treatment resulted in the increase in phosphorus-containing groups on the surface of the activated carbon, leading to improvements in Cu (II) adsorption capacity. Chen, Pan, and Chen [29] successfully used DBD plasma for regeneration of activated carbon, after sorption of dimethyl sulfide, losing only a couple of percentage points of the sorption capacity (approx. 62 mg of C_2H_6S per g of activated carbon), after 10 regeneration cycles, each taking 25 min.

2. Materials and Methods

2.1. Brewer's Spent Grain Sample

Studies were conducted on two materials, hydrochar from Brewer's Spent Grain (BSG-HC) and commercial activated carbon (AC). The initial test material from which BSG-HC was made was BSG malt. As characteristics of BSG is always strongly dependent on both malt and brewing process [3,5], the BSG was obtained in a controlled manner, as a side product from the brewery on the Wroclaw University of Science and Technology's campus (Poland). An amount of 18 kg pilsner malt, 2.45 kg Munich malt, and 0.85 kg dark malt were used to create the beer (all malts were purchased from Viking Malt malthouse). A total of 100 dm^3 was used in each batch. The mashing regime was 15 min at a temperature of 336 K followed by 20 min in 346 K. The spent grain sample was taken after the mashing process and subsequently dried.

2.2. Hydrothermal Carbonization

A diagram of the experimental setup (Figure 1) shows both the autoclave rig as well as the hydraulic press, which was used for the subsequent dewatering of the hydrochars. The autoclave was loaded with distilled water and wet spent grain to achieve a water to dry biomass ratio of 10:1, which was computed as the mass/mass ratio of total water (distilled water and moisture in the biomass) to the mass of the dry-processed feedstock. The dry mass of the processed sample was around 400 g. The freeboard of the autoclave was purged with nitrogen of technical purity after adding both biomass and water. A heating mantle with band heaters was used to heat the autoclave vessel. A K-type thermocouple coupled to a PLC controller was used to measure the temperature. The temperature of 473 K was chosen as the set point temperature since it is a reasonably typical temperature for the HTC process, with most of the literature results being reported for the temperature range of 473 K to 533 K. [8,23,30]. Residence time in the reactor was 150 min. After the autoclave reached the specified point temperature, the timer began to run. The heating mantle was turned off after 2.5 h, and the arrangement was allowed to cool.
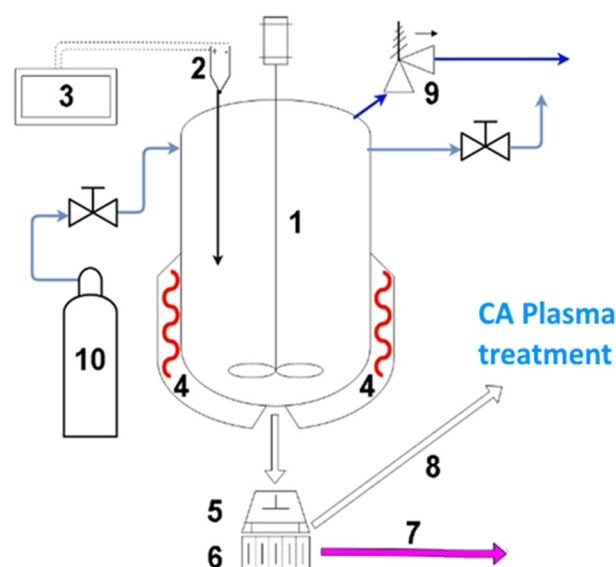
Figure 1. Diagram of the test rig, used for hydrothermal carbonization of the spent grain (1—Autoclave; 2—type K thermocouple; 3—PLC controller; 4—heating mantle, with band heaters; 5—hydraulic press; 6—filter; 7—liquid, after mechanical dewatering; 8—hydrochar from Brewer's Spent Grain, after mechanical dewatering; 9—pressure relief valve; 10—nitrogen for purging).

2.3. Cold Atmospheric Plasma Jet Treatment

Cold atmospheric plasma sometimes called non-thermal plasma is a partially ionized gas with ions, electrons, and uncharged particles such as molecules, atoms, and radicals. Parameters that differentiate hot and cold plasma are pressure and time of discharge. In a hot plasma, electrons are in thermodynamic equilibrium with ions, whereas in a cold plasma the electrons are (generally) more energetic than ions. Cold plasma is generated by short pulse discharges that happen at a pressure lower than ambient. What is unique in the phenomena of cold plasma is that electrons are much hotter than the heavy particles that are at room temperature. In the place of application, the temperature is less than 313 K. Gases that can be ionized are helium, argon, nitrogen, heliox, and air, whereas the methods to produce cold plasma are: corona discharge, dielectric barrier discharge (DBD), gliding arc discharge and radiofrequency plasma.

Both hydrochar (BSG-HC) and activated carbon (AC) were subjected to cold plasma activation. Dielectric barrier discharge was achieved using argon and helium as plasma forming gases (Figure 2). BSG-HC was treated with an 18 W helium plasma jet and a 13 W argon plasma jet, whereas AC was treated with a 20 W He and 13 W Ar plasma jet. Operating pressure was close to atmospheric, i.e., it was atmospheric at the outlet of the jet and close to 1 bar at the outlet of the pressure reducing regulator on the gas bottle, both for Ar and He. The residence time in the plasma activation was t_{res} = 3 min.
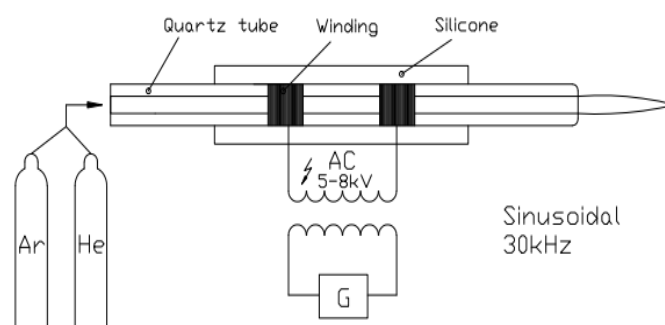

Figure 2. Bespoke rig for cold atmospheric plasma activation.

Reference (BSG-HC) and plasma-activated hydrochars (BSG-HC/He and BSG-HC/Ar), as well as activated carbon samples before (AC) and after plasma treatment (AC/He and AC/Ar) were structurally characterized by low-pressure nitrogen adsorption (LPNA) at 77 K. A volumetric analyzer ASAP 2020 (Micromeritics) was used for measurement. The analysis was performed based on a continuous control of the volume of adsorbed gas as a function of set pressure. The measurement was carried out at a relative pressure of $0 < p/p_0 < 1$, corresponding to an absolute pressure of 0–0.1 MPa. After each pressure step, the equilibrium sorption point was obtained and the measurement resulted in adsorption and desorption isotherms.

Since the materials studied differed significantly in structure, different theoretical models were used to characterize their pore spaces. According to the Langmuir model, the adsorbate molecules form a single layer on the adsorbent surface. This occurs in typically microporous materials. The Langmuir model is expressed by the formula:

$$a(p) = \frac{A_L \cdot B \cdot p}{1 + B \cdot p},$$ (1)

where: $a(p)$ is the sorption capacity at pressure p, (cm^3/g); A_L is the total monolayer sorption capacity, (cm^3/g); B is the inverse of half-pressure, $(1/MPa)$; p is the absolute pressure, (MPa).

For mesoporous and macroporous materials, the Brunauer–Emmett–Teller (BET) model is used, where multilayer adsorption occurs on the surface:

$$a(p) = \frac{A_{BET} \cdot C \cdot \frac{p}{p_0}}{\left(1 - \frac{p}{p_0}\right) \cdot \left[1 + (C-1) \cdot \frac{p}{p_0}\right]},$$ (2)

where: $a(p)$ is the sorption capacity at pressure p, (cm^3/g), A_{BET} is total sorption capacity according to the BET model, (cm^3/g), C is the constant of adsorption balance in the BET model, $(-)$, p/p_0 is relative pressure, $(-)$.

The structural parameters: specific surface area, total pore volume, average pore size and pore size distribution were determined from the sorption points and models. The specific surface area was determined from the total sorption capacities (A_{BET}, A_L) from the formula:

$$SSA = A \cdot \omega \cdot N_A,$$ (3)

where: SSA is the specific surface area according to the BET or Langmuir model, (m^2/g), A is total sorption capacity according to the BET or Langmuir model, (cm^3/g), ω is the surface occupied by a single molecule of adsorbate in the monomolecular layer, (nm^2), and N_A is Avogadro's number $(1/mol)$.

Other structural parameters were determined using MicroActive 5.01 software (Micromeritics). The total volume of mesopores and macropores was determined according to the Barrett–Joyner–Halenda (BJH) model. Calculations for Carbon Black STSA type materials were used here. The volume and distribution of micropores were determined according to the Density Functional Theory (DFT) model. For BSG-HC materials, model type N_2 @ 77 K on Carbon, Split Pores was used, whereas for AC materials, model type N_2 @ 77 K, Cylindrical Pores in an Oxide Surface was used.

Images of samples were taken using an Eclipse LV100N POL motorized polarizing microscope (NIKON) with a CFI60 Infinity optical system. Analyses were performed under transmitted light at magnifications of $100\times$ and $200\times$. Each image presented is a composite of several hundred images obtained during the 3D analysis of each sample, and Figures show projections in the XYZ plane.

3. Results

Low-pressure sorption studies resulted in sorption isotherms based on BSG hydrochars (BSG-HC), which were subsequently treated with helium (BSG-HC/He) and argon (BSG-

HC/Ar) plasma for 3 min. Similar treatment time (1 min) has been applied by Xu et al. [43] for cold plasma treatment of garden waste. Moreover, Benoit et al. [44] observed fructose in the solution collected after 7 min of non-thermal atmospheric plasma treatment, indicating that some changes can occur after such residence time, when looking from a chemical perspective. The isotherms are shown in Figure 3A. The shape of the isotherms is type III according to IUPAC, indicating that the materials studied are weakly porous or non-porous. In plasma treated samples (BSG-HC/He, BSG-HC/Ar), the sorption of N_2 is clearly higher, especially when $p/p_0 > 0.8$. This may indicate the opening of new mesopores and macropores as a result of plasma treatment. The total sorption capacity, from a value of 0.46 cm^3 N_2/g before plasma treatment, increased to 3.47 cm^3 N_2/g after He plasma treatment and to 5.32 cm^3 N_2/g after Ar treatment. In commercial activated carbons (ACs), the plasma effect was not very large. Type I isotherms were obtained, indicating the microporous and partially mesoporous structure of the material (Figure 3B), and hysteresis loops in the range $0.5 < p/p_0 < 1$ were obtained. The plasma treatment had a positive effect. The shape of the isotherms of activated materials did not change, but the total sorption capacity increased from 307.2 cm^3/g before plasma treatment to 351.9 cm^3/g and 375.5 cm^3/g after cold plasma activation with Ar and He, respectively.
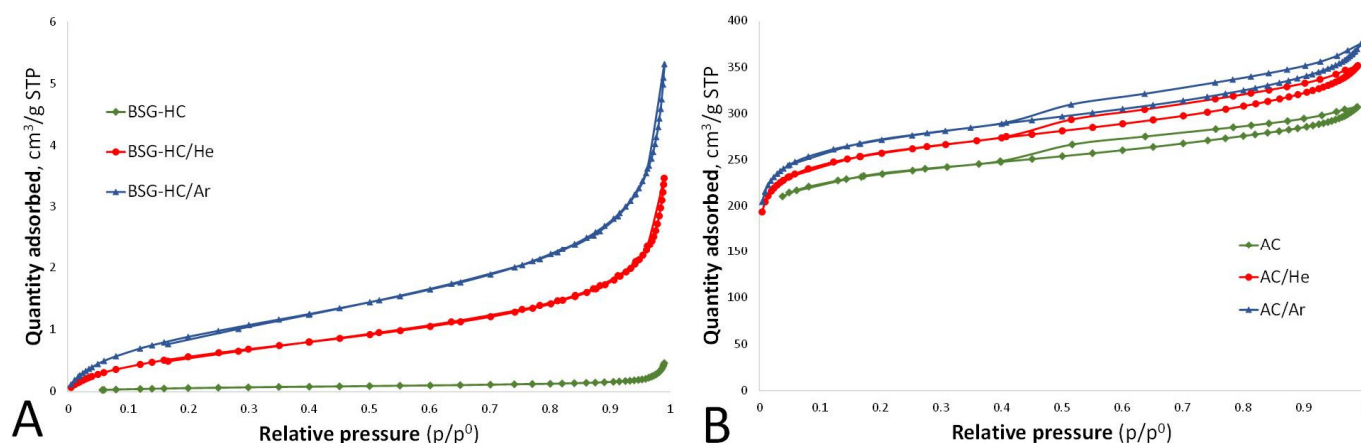

Figure 3. N_2 adsorption isotherms: (**A**) hydrochars from Brewer's Spent Grain (BSG-HC), (**B**) activated carbons (AC).

Table 1 contains the values of structural parameters calculated from N_2 adsorption isotherms. The BET specific surface area of BSG-HC materials was in the range of 0.25–3.70 m^2/g and was highest in the material after argon activation (BSG-HC/Ar). Here, a high degree of fit of the BET model to the isotherm obtained from the equilibrium points was obtained. In activated carbons, argon treatment increased SSA_{BET}, from 731.3 m^2/g (AC) to 939.7 m^2/g, whereas SSA_L increased from 1077.5 m^2/g to 1417.7 m^2/g (AC/Ar). For AC materials, a better fit of the Langmuir isotherm to the equilibrium points of N_2 sorption was obtained.

To determine how the volume changed in the range of different pore sizes, the total pore volume was determined, and pore size distributions (PSDs) were performed based on two different models. Using the DFT model, it was determined that the plasma treatment affected the narrower pores (Figure 4A). No pores with diameters below 1.3 nm were detected, and in pores with diameters of 1.3–15.0 nm the volume increase was relatively high. The total pore volume increased from 0.15 mm^3/g (BSG-HC) to 3.87 mm^3/g after argon plasma treatment. According to the BJH model, which is dedicated to mesopores, in BSG-HC materials, plasma treatment resulted in a volume increase in the pore range from 1.9 nm to 164 nm (Figure 4B). Although a relatively high increase in total pore volume was also obtained (Table 1), this parameter was no more than 7.6 mm^3/g (BSG-HC/Ar). The average pore diameter here was 8.7–11.7 nm.

Table 1. Structural parameters.

Symbol	BSG-HC	BSG-HC/He	BSG-HC/Ar	AC	AC/He	AC/Ar
a (0.1 MPa)	0.46	3.47	5.32	307.2	351.9	375.5
SSA_{BET}	0.25	2.38	3.70	731.3	808.1	939.7
A_{BET}	0.06	0.55	0.85	-	-	-
SSA_L	0.61	7.14	10.57	1077.5	1311.3	1417.7
A_L	-	-	-	247.4	301.2	325.7
V_{BJH}	0.65	5.01	7.59	173.2	224.3	235.7
D_{BJH}	11.7	9.0	8.7	4.6	4.6	4.6
V_{DFT}	0	0	0	353.68	383.45	405.56
Vt_{DFT}	0.15	2.49	3.87	421.56	481.52	508.02

a (0.1 MPa) is sorption capacity at 0.1 MPa, (cm^3/g STP); SSA_{BET}, is BET surface area, (m^2/g); A_{BET} is total sorption capacity according to the BET model, (cm^3/g); SSA_L is Langmuir surface area, (m^2/g); A_L is total sorption capacity according to the Langmuir model, (cm^3/g); V_{BJH} is BJH total pore volume, (mm^3/g); D_{BJH} is adsorption average pore diameter, (nm); V_{DFT} is DFT pore volume in pores < 1.4 nm, (mm^3/g); Vt_{DFT} is DFT total pore volume in pores, (mm^3/g).
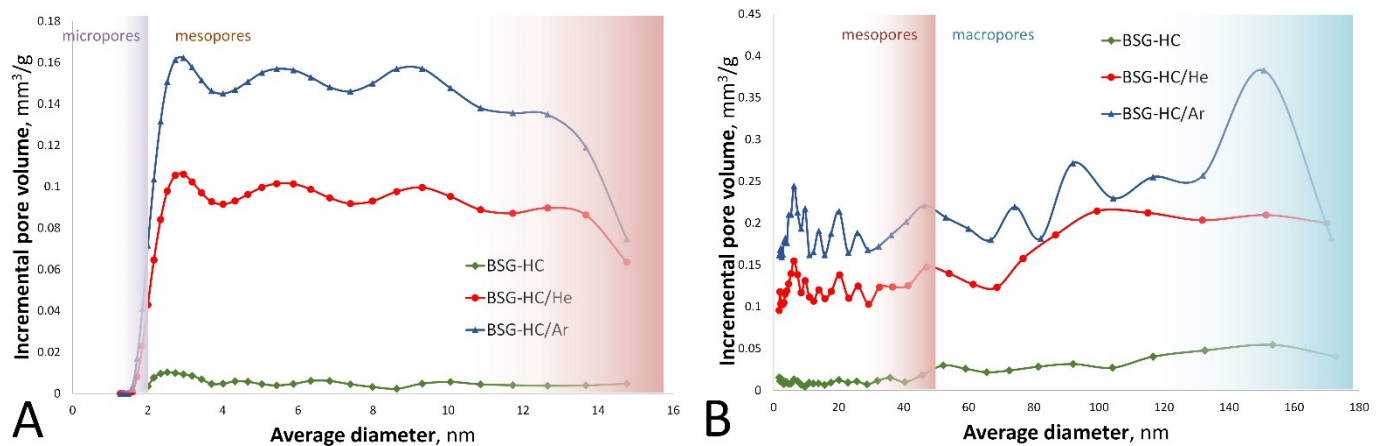
Figure 4. Pore size distribution of BSG-HC: (**A**) according to DFT model (**B**) according to BJH model.

A similar observation was made when characterizing activated carbons. In AC materials, the PSD according to the BJH model had similar patterns, and the highest volume was obtained in pores with diameters up to 20 nm. Plasma treatment resulted in an increase in total pore volume (Table 1) from 173.2 mm^3/g (AC) to 235.7 mm^3/g (AC/Ar). According to the DFT model, dedicated to the finest pores, the total pore volume increased from 422 mm^3/g (AC) to 508 mm^3/g (AC/Ar). Figure 5 presents the PSD results for AC according to the DFT (Figure 5A) and BJH (Figure 5B) models.
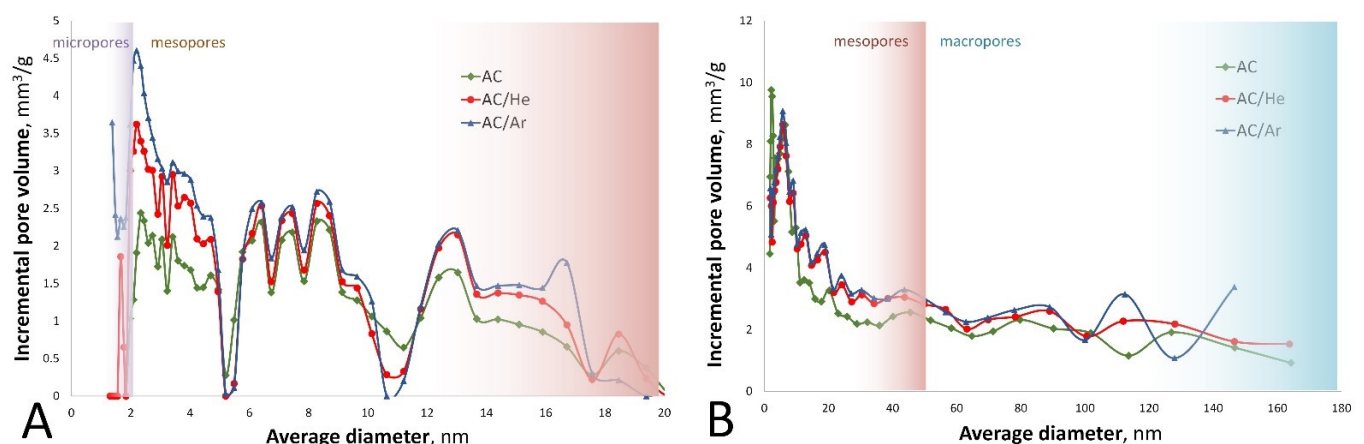
Figure 5. Pore size distribution of AC: (**A**) according to DFT model, (**B**) according to BJH model.

For observation purposes, microscopic images of both materials after helium and argon activation were taken. The photos are presented in Figure 6. The materials studied after activation looked similar microscopically. They had different textures and particles in the form of agglomerates (Figure 6C,F).
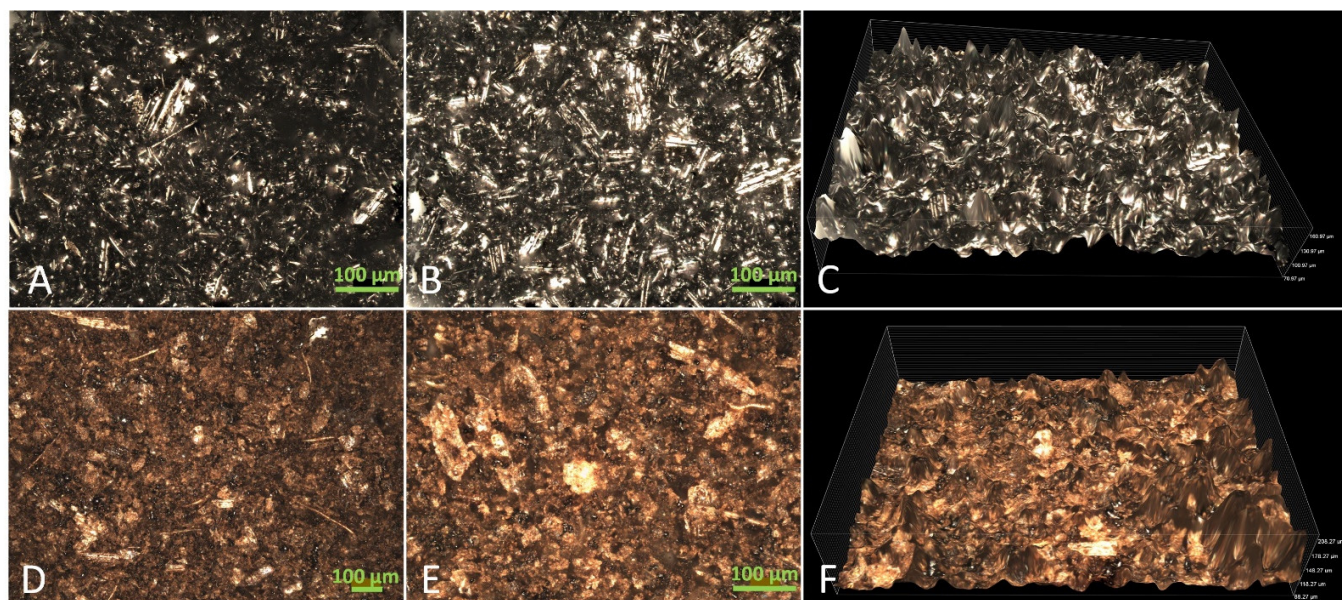

Figure 6. Images of samples: (**A**) AC/He, (**B**) AC/Ar, (**C**) AC/Ar, (**D**) BSG-HC/He, (**E**) BSG-HC/Ar, (**F**) BSG-HC/Ar.

Based on the study of two different materials (BSG-HC and AC), it was observed that the choice of plasma gas is important in terms of increasing the pore structure of the materials and potentially increasing the sorption capacity. In the presented study, a different plasma jet power was used to generate plasmas using argon and helium. This was determined by the need to maintain plasma jet stability in each of the two cases. It was not possible to maintain stable jet operation at the same power for two different gases due to their respective properties. In addition, a higher sorption capacity was obtained for the Ar plasma, which used a relatively lower power of 13 W compared with 17 W for the He plasma.

To assess the effect of the activations used on the BSG-HC and AC, the ratio of the quantity adsorbed of the activated samples relative to the samples without activation was determined. The summary in Figure 7 indicates that, irrespective of the plasma gas used, activation of the hydrochars is effective. Considering the sorption capacity parameters a (0.1 MPa), the ratio of the values of this parameter before plasmaing to the values after plasmaing in BSG-HC was 7.5 for helium plasma and 11.6 for argon plasma. These are very high values, which show that the gas adsorption efficiency increased more than seven times and more than eleven times after activation, respectively. Even higher values were obtained for the pore volume parameters V_{BJH} and specific surface area. SSA_{BET} increased nearly ten-fold (He use) and nearly fifteen-fold (Ar use) after activation. Despite the lower plasma power, the Ar treatment resulted in a greater increase in the values of all pore space parameters in BSG-HC.
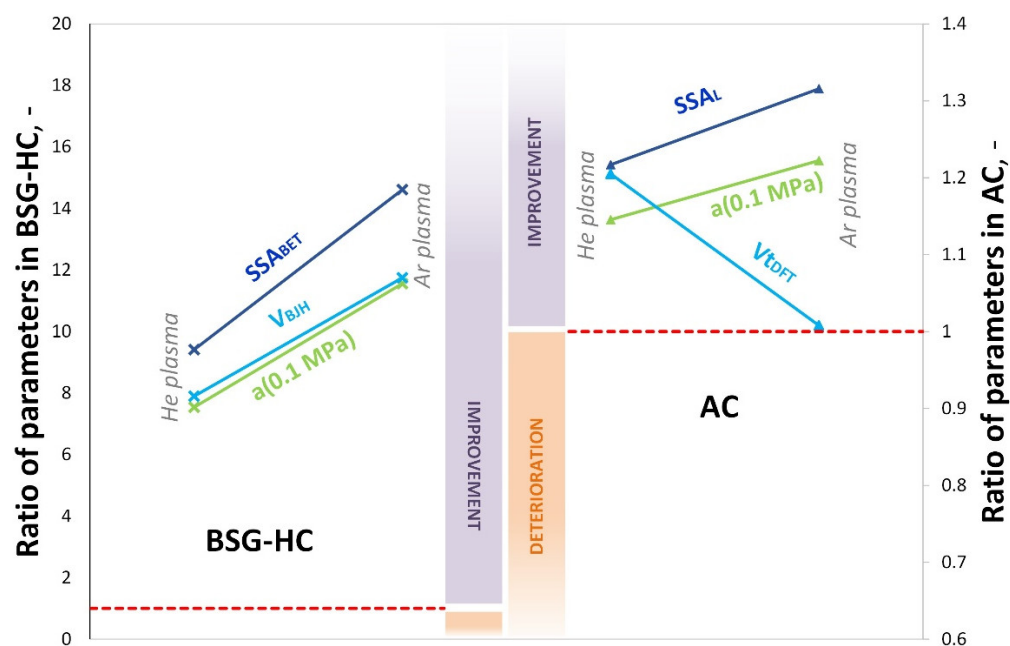
Figure 7. Relationship diagram of the structural parameters in BSG-HC and AC.

Activation of activated carbon did not have such high effects, but the effect was positive in each case. For the sorption capacity parameter *a* (0.1 MPa), the ratios before and after plasma treatment with helium and argon were 1.1 and 1.2, respectively. For the specific surface area of SSA_L, ratios of 1.2 (He use) and 1.3 (Ar use) were obtained. In opposite to BSG-HC, no significant effect of plasma type was observed for the reference activated carbons. The correlations are shown in Figure 7.

Since the reference activated carbon was subjected to a state-of-the-art activation process (activated carbon was purchased commercially), it seems plausible to suspect that plasma interacted with the parts of hydrochars that could be relatively easy to decompose, such as secondary hydrochars, which are typically produced by precipitation and condensation of organics in the effluent [45].

4. Conclusions

Overall, treatment with cold atmospheric (CA) argon and helium plasma was not sufficient to create a high of the micro and mesopores volume to make BSG hydrochars comparable with commercially available activated carbons. Therefore, it seems that an additional step would be needed for successful activation, e.g., change of plasma gas and use of some chemical additive. Nonetheless, it should not be overlooked that CA plasma can exhibit a stronger influence, depending on the plasma gas. As interaction with secondary hydrochars seems to be the most plausible route, possibilities regarding functionalization of the surface, using CA plasma, seem to be a good recommendation for further research.

Author Contributions: Conceptualization: K.K., H.P.-K. and N.S.; methodology: K.K. and A.G.; validation: N.S., M.K., R.G. and A.K.J.; formal analysis: A.G. and A.A.; investigation: K.K., A.G., M.S.-T., T.C. and M.J.; resources: K.K., H.P.-K., N.S., T.C. and T.H.; data curation: A.A., M.K., T.H. and R.G.; writing—original draft preparation: Ł.N., A.G., M.J., V. and R.G.; writing—review and editing: H.P.-K., M.K., N.S., T.H., M.O. and R.G.; visualization, K.K., M.O. and R.G.; supervision: K.K., H.P.-K., A.A. and T.H.; project administration: K.K. and M.O.; funding acquisition: K.K., M.O. and N.S. All authors have read and agreed to the published version of the manuscript.

Conflicts of Interest: The authors declare no conflict of interest. The funders had no role in the design of the study; in the collection, analyses, or interpretation of data; in the writing of the manuscript; or in the decision to publish the results.

References

1. Beer Production Worldwide from 1998 to 2020 (in Billion Hectoliters). Available online: https://www.statista.com/statistics/270275/worldwide-beer-production/ (accessed on 1 June 2022).
2. Bentzen, J.; Smith, V. Structural Changes in the Consumption of Beer, Wine and Spirits in OECD Countries from 1961 to 2014. *Beverages* **2018**, *4*, 8. [CrossRef]
3. Jackowski, M.; Niedzwiecki, L.; Jagiełło, K.; Uchańska, O.; Trusek, A. Brewer's Spent Grains—Valuable Beer Industry by-Product. *Biomolecules* **2020**, *10*, 1669. [CrossRef] [PubMed]
4. Enweremadu, C.; Waheed, M.A.; Adekunle, A.A.; Adeala, A. The Energy Potential of Brewer's Spent Grain for Breweries in Nigeria. *Eng. Appl. Sci.* **2008**, *3*, 175–177.
5. Jackowski, M.; Niedzwiecki, L.; Lech, M.; Wnukowski, M.; Arora, A.; Tkaczuk-Serafin, M.; Baranowski, M.; Krochmalny, K.; Veetil, V.K.; Seruga, P.; et al. HTC of Wet Residues of the Brewing Process: Comprehensive Characterization of Produced Beer, Spent Grain and Valorized Residues. *Energies* **2020**, *13*, 2058. [CrossRef]
6. Jackowski, M.; Semba, D.; Trusek, A.; Wnukowski, M.; Niedzwiecki, L.; Baranowski, M.; Krochmalny, K.; Pawlak-Kruczek, H. Hydrothermal Carbonization of Brewery's Spent Grains for the Production of Solid Biofuels. *Beverages* **2019**, *5*, 12. [CrossRef]
7. Mokrzycki, J.; Lorenc-Grabowska, E.; Kordek-Khalil, K.; Rutkowski, P. Hydrothermal and Pyrolytic Biochars from Waste Milk Thistle (Silybum Marianum) Extrudates as Precursors for Production of Effective Isoproturon Adsorbents. *J. Water Process Eng.* **2020**, *37*, 101459. [CrossRef]
8. Mlonka-Mędrala, A.; Sieradzka, M.; Magdziarz, A. Thermal Upgrading of Hydrochar from Anaerobic Digestion of Municipal Solid Waste Organic Fraction. *Fuel* **2022**, *324*, 124435. [CrossRef]
9. Numviyimana, C.; Warchoł, J.; Khalaf, N.; Leahy, J.J.; Chojnacka, K. Phosphorus Recovery as Struvite from Hydrothermal Carbonization Liquor of Chemically Produced Dairy Sludge by Extraction and Precipitation. *J. Environ. Chem. Eng.* **2022**, *10*, 106947. [CrossRef]
10. Aragón-Briceño, C.I.; Ross, A.B.; Camargo-Valero, M.A. Mass and Energy Integration Study of Hydrothermal Carbonization with Anaerobic Digestion of Sewage Sludge. *Renew. Energy* **2021**, *167*, 473–483. [CrossRef]
11. Wilk, M.; Śliz, M.; Gajek, M. The Effects of Hydrothermal Carbonization Operating Parameters on High-Value Hydrochar Derived from Beet Pulp. *Renew. Energy* **2021**, *177*, 216–228. [CrossRef]
12. Reza, M.T.; Lynam, J.G.; Uddin, M.H.; Coronella, C.J. Hydrothermal Carbonization: Fate of Inorganics. *Biomass Bioenergy* **2013**, *49*, 86–94. [CrossRef]
13. Moscicki, K.J.; Niedzwiecki, L.; Owczarek, P.; Wnukowski, M. Commoditization of Wet and High Ash Biomass: Wet Torrefaction—A Review. *J. Power Technol.* **2017**, *97*, 354–369.
14. Funke, A.; Ziegler, F. Hydrothermal Carbonisation of Biomass: A Summary and Discussion of Chemical Mechanisms for Process Engineering. *Biofuels Bioprod. Biorefin.* **2010**, *4*, 160–177. [CrossRef]
15. Reza, M.T.; Andert, J.; Wirth, B.; Busch, D.; Pielert, J.; Lynam, J.G.; Mumme, J. Hydrothermal Carbonization of Biomass for Energy and Crop Production. *Appl. Bioenergy* **2014**, *1*, 11–29. [CrossRef]
16. Reza, M.T.; Yan, W.; Uddin, M.H.; Lynam, J.G.; Hoekman, S.K.; Coronella, C.J.; Vásquez, V.R. Reaction Kinetics of Hydrothermal Carbonization of Loblolly Pine. *Bioresour. Technol.* **2013**, *139*, 161–169. [CrossRef]
17. Tungal, R.; Shende, R.V. Hydrothermal Liquefaction of Pinewood (Pinus Ponderosa) for H_2, Biocrude and Bio-Oil Generation. *Appl. Energy* **2014**, *134*, 401–412. [CrossRef]
18. Nan, W.; Shende, A.R.; Shannon, J.; Shende, R.V. Insight into Catalytic Hydrothermal Liquefaction of Cardboard for Biofuels Production. *Energy Fuels* **2016**, *30*, 4933–4944. [CrossRef]
19. Shende, R.; Tungal, R. Subcritical Aqueous Phase Reforming of Wastepaper for Biocrude and H_2 Generation. *Energy Fuels* **2013**, *27*, 3194–3203. [CrossRef]
20. Funke, A.; Ziegler, F. Heat of Reaction Measurements for Hydrothermal Carbonization of Biomass. *Bioresour. Technol.* **2011**, *102*, 7595–7598. [CrossRef]
21. Acharjee, T.C.; Coronella, C.J.; Vasquez, V.R. Effect of Thermal Pretreatment on Equilibrium Moisture Content of Lignocellulosic Biomass. *Bioresour. Technol.* **2011**, *102*, 4849–4854. [CrossRef]
22. Ahmed, M.; Andreottola, G.; Elagroudy, S.; Negm, M.S.; Fiori, L. Coupling Hydrothermal Carbonization and Anaerobic Digestion for Sewage Digestate Management: Influence of Hydrothermal Treatment Time on Dewaterability and Bio-Methane Production. *J. Environ. Manag.* **2021**, *281*, 111910. [CrossRef] [PubMed]
23. Gao, N.; Li, Z.; Quan, C.; Miskolczi, N.; Egedy, A. A New Method Combining Hydrothermal Carbonization and Mechanical Compression In-Situ for Sewage Sludge Dewatering: Bench-Scale Verification. *J. Anal. Appl. Pyrolysis* **2019**, *139*, 187–195. [CrossRef]
24. Urbanowska, A.; Kabsch-Korbutowicz, M.; Aragon-Briceño, C.; Wnukowski, M.; Pożarlik, A.; Niedzwiecki, L.; Baranowski, M.; Czerep, M.; Seruga, P.; Pawlak-Kruczek, H.; et al. Cascade Membrane System for Separation of Water and Organics from Liquid By-Products of HTC of the Agricultural Digestate—Evaluation of Performance. *Energies* **2021**, *14*, 4752. [CrossRef]

25. Urbanowska, A.; Kabsch-Korbutowicz, M.; Wnukowski, M.; Seruga, P.; Baranowski, M.; Pawlak-Kruczek, H.; Serafin-Tkaczuk, M.; Krochmalny, K.; Niedzwiecki, L. Treatment of Liquid By-Products of Hydrothermal Carbonization (HTC) of Agricultural Digestate Using Membrane Separation. *Energies* **2020**, *13*, 262. [CrossRef]

26. Aragón-Briceño, C.; Ross, A.B.B.; Camargo-Valero, M.A.A. Evaluation and Comparison of Product Yields and Bio-Methane Potential in Sewage Digestate Following Hydrothermal Treatment. *Appl. Energy* **2017**, *208*, 1357–1369. [CrossRef]

27. Ferrentino, R.; Merzari, F.; Fiori, L.; Andreottola, G. Coupling Hydrothermal Carbonization with Anaerobic Digestion for Sewage Sludge Treatment: Influence of HTC Liquor and Hydrochar on Biomethane Production. *Energies* **2020**, *13*, 6262. [CrossRef]

28. Sobek, S.; Tran, Q.K.; Junga, R.; Werle, S. Hydrothermal Carbonization of the Waste Straw: A Study of the Biomass Transient Heating Behavior and Solid Products Combustion Kinetics. *Fuel* **2022**, *314*, 122725. [CrossRef]

29. Wnukowski, M.; Owczarek, P.; Niedźwiecki, Ł. Wet Torrefaction of Miscanthus—Characterization of Hydrochars in View of Handling, Storage and Combustion Properties. *J. Ecol. Eng.* **2015**, *16*, 161–167. [CrossRef]

30. Sharma, H.B.; Dubey, B.K. Binderless Fuel Pellets from Hydrothermal Carbonization of Municipal Yard Waste: Effect of Severity Factor on the Hydrochar Pellets Properties. *J. Clean. Prod.* **2020**, *277*, 124295. [CrossRef]

31. Surup, G.R.; Leahy, J.J.; Timko, M.T.; Trubetskaya, A. Hydrothermal Carbonization of Olive Wastes to Produce Renewable, Binder-Free Pellets for Use as Metallurgical Reducing Agents. *Renew. Energy* **2020**, *155*, 347–357. [CrossRef]

32. Murillo, H.A.; Díaz-Robles, L.A.; Santander, R.E.; Cubillos, F.A. Conversion of Residual Biomass into Valuable Biofuels by Co-Hydrothermal Carbonization for Utilization in Household Pellet Stoves. *Biomass Bioenergy* **2021**, *151*, 106153. [CrossRef]

33. Tang, H.; Duan, Y.; Zhu, C.; Li, C.; She, M.; Zhou, Q.; Cai, L. Characteristics of a Biomass-Based Sorbent Trap and Its Application to Coal-Fired Flue Gas Mercury Emission Monitoring. *Int. J. Coal Geol.* **2017**, *170*, 19–27. [CrossRef]

34. Karimi, M.; Shirzad, M.; Silva, J.A.C.; Rodrigues, A.E. Biomass/Biochar Carbon Materials for CO_2 Capture and Sequestration by Cyclic Adsorption Processes: A Review and Prospects for Future Directions. *J. CO_2 Util.* **2022**, *57*, 101890. [CrossRef]

35. Pajdak, A.; Skoczylas, N.; Szymanek, A.; Lutyński, M.; Sakiewicz, P. Sorption of CO_2 and CH_4 on Raw and Calcined Halloysite—Structural and Pore Characterization Study. *Materials* **2020**, *13*, 917. [CrossRef] [PubMed]

36. Zhang, M.; Liang, X.; Chen, H. A Novel Effective Approach for Synergistic NO Reduction during the Carbonation Process by Biomass-Modified Calcium-Based Sorbents. *Chem. Eng. J.* **2022**, *439*, 135795. [CrossRef]

37. Pajdak, A.; Walawska, B.; Szymanek, A. The Effect of Structure Modification of Sodium Compounds on the SO_2 and HCl Removal Efficiency from Fumes in the Conditions of Circulating Fluidised Bed. *Chem. Biochem. Eng. Q.* **2017**, *31*, 261–273. [CrossRef]

38. Pajdak, A. Porównanie Kinetyki Sorpcji Wodoru w Stopie Metalicznym LaNi5 i Wielościennych Nanorurkach Węglowych. *Przem. Chem.* **2018**, *1*, 145–148. [CrossRef]

39. Pajdak, A.; Skoczylas, N.; Dębski, A.; Grzegorek, J.; Maziarz, W.; Kudasik, M. CO_2 and CH_4 Sorption on Carbon Nanomaterials and Coals—Comparative Characteristics. *J. Nat. Gas Sci. Eng.* **2019**, *72*, 103003. [CrossRef]

40. Skiba, M.; Młynarczuk, M. Estimation of Coal's Sorption Parameters Using Artificial Neural Networks. *Materials* **2020**, *13*, 5422. [CrossRef]

41. Ng, C.; Marshall, W.E.; Rao, R.M.; Bansode, R.R.; Losso, J.N. Activated Carbon from Pecan Shell: Process Description and Economic Analysis. *Ind. Crops Prod.* **2003**, *17*, 209–217. [CrossRef]

42. Konno, K.; Oike, Y.; Ohba, Y.; Sasaki, O.; Takiguchi, Y.; Onoe, K.; Yamaguchi, T. Short-Time Preparation of NaOH-Activated Carbon from Sugar Cane Bagasse Using Microwave Plasma Heating. *Green Sustain. Chem.* **2017**, *7*, 259–269. [CrossRef]

43. Xu, Z.; Ma, Y.; Li, Y.; Li, G.; Nghiem, L.; Luo, W. Comparison between Cold Plasma, Ultrasonication, and Alkaline Hydrogen Peroxide Pretreatments of Garden Waste to Enhance Humification in Subsequent Composting with Kitchen Waste: Performance and Mechanisms. *SSRN Electron. J.* **2022**, *354*, 127228. [CrossRef]

44. Benoit, M.; Rodrigues, A.; De Oliveira Vigier, K.; Fourré, E.; Barrault, J.; Tatibouët, J.-M.; Jérôme, F. Combination of Ball-Milling and Non-Thermal Atmospheric Plasma as Physical Treatments for the Saccharification of Microcrystalline Cellulose. *Green Chem.* **2012**, *14*, 2212. [CrossRef]

45. Picone, A.; Volpe, M.; Messineo, A. Process Water Recirculation during Hydrothermal Carbonization of Waste Biomass: Current Knowledge and Challenges. *Energies* **2021**, *14*, 2962. [CrossRef]